GAS GIANT PLANETS

Peering through Jupiter's clouds with radio spectral imaging

Imke de Pater,[1,2,3*] R. J. Sault,[4] Bryan Butler,[5] David DeBoer,[1] Michael H. Wong[1]

Radio wavelengths can probe altitudes in Jupiter's atmosphere below its visible cloud layers. We used the Very Large Array to map this unexplored region down to ~8 bar, ~100 kilometers below the visible clouds. Our maps reveal a dynamically active planet at pressures less than 2 to 3 bar. A radio-hot belt exists, consisting of relatively transparent regions (a low ammonia concentration, NH_3 being the dominant source of opacity) probing depths to over ~8 bar; these regions probably coincide with 5-micrometer hot spots. Just to the south we distinguish an equatorial wave, bringing up ammonia gas from Jupiter's deep atmosphere. This wave has been theorized to produce the 5-micrometer hot spots; we observed the predicted radio counterpart of such hot spots.

Despite the fact that Jupiter has been observed for decades from the ground and in situ by spacecraft, questions remain about its bulk composition and global atmospheric dynamics. Much information on Jupiter's deep atmospheric composition was obtained, however, by the probe on the Galileo spacecraft, even though it descended in a 5-μm hot spot; i.e., a region that is "dry": devoid of clouds and condensable gases. The deep (>8 bar) mole fractions of NH_3 and H_2S were found to be enriched by a factor of 3 to 5 over the solar composition (*1*). This was several times higher than NH_3 mole fractions derived from radio spectra globally at higher altitudes [pressure (P) < 4 bar] and locally over the North Equatorial Belt (NEB) and Equatorial Zone (EZ) (*2*). With NH_3 being the dominant source of opacity at radio wavelengths, this difference could not be reconciled. A longitude-resolved global radio map of Jupiter (*3*), constructed from data at a single frequency of 15 GHz, showed regions similar to 5-μm hot spots with depleted NH_3 down to $P > 5$ bar but no regions with NH_3 mole fractions equal to the Galileo-derived deep abundance. A two-layer model of Jupiter's cloud-layer circulation was developed (*4*), explaining that NH_3 could be globally depleted (at 0.5 to 4 bar) if upward transport occurred primarily in precipitating thunderstorms. Our observations show that a two-layer circulation pattern is not needed to explain the NH_3 concentrations, at least in the equatorial region.

We used the upgraded Karl G. Jansky Very Large Array (VLA) (Table 1) to observe Jupiter over the full frequency range from 4 to 18 GHz (1.7 to 7 cm) (*5*). Our new maps have a sensitivity up to an order of magnitude higher than the previously obtained longitude-resolved 15-GHz map, and achieve a 2 to 5 times higher spatial resolution (~1300 km at disk center in the new 15-GHz map versus ~5000 km in the previous map). These maps probe depths in Jupiter's atmosphere between ~0.5 and ~10 bar, a vertical range of over 100 km (*2*, *6*), covering the altitude range where Jupiter's main cloud layers are formed (Fig. 1) (*7*).

Figure 2, A to D, shows radio maps averaged over 12 to 18 GHz, 8 to 12 GHz, and 4 to 8 GHz, after subtraction of a best-fit uniform limb-darkened disk (*5*). Panels E to H show Jupiter's almost-simultaneous appearance at visible wavelengths for comparison (*8*). A wealth of structure is visible in each radio map, which is easily distinguished from some "ripples" and large-scale dark and light areas that are instrumental artefacts. In panel D, some of these large-scale patterns are caused by Jupiter's synchrotron radiation (*2*, *5*). Brightness temperatures (T_bs) in excess of the best-fit subtracted disk show up as bright (light-colored) regions, and lower temperatures are dark. A higher T_b indicates probing deeper levels in the atmosphere and hence suggests a low atmospheric opacity (i.e., low NH_3 concentration), and dark regions correspond to a high opacity. Our observations thus provide the three-dimensional distribution of NH_3 gas, which we use to trace dynamics, assuming the following: In parcels of rising air, NH_3 is enriched above solar levels, or within and above the NH_3 ice layer, NH_3 is saturated. Descending flows that originate at or above the NH_3 cloud base carry depleted ammonia with respect to the deep abundance.

Historically, the zone-belt structures at visible, 5-μm, and radio wavelengths were thought to be well correlated. Brownish belts were thought to correspond to bands that are bright at 5 μm and in the radio, and whiter zones to bands that were dark at 5 μm and in the radio (*9*). A detailed comparison of the images in Fig. 2, however, reveals important refinements to this view. A radio-hot belt is visible right at the interface between the NEB and EZ, on the north side of the 7.8°N eastward jet. The northern and southern edges of the South Equatorial Belt (SEB) are radio-bright, whereas the darkest reddish interior is radio-dark. Several radio-bright bands are seen between 40° and 60°S, which do not necessarily seem to be connected to optical counterparts. The radio-hot belt at ~8°N contains structure at the limits of our resolution, as well as bright regions elongated in longitude. Elongated radio-bright regions coincide with the dark-gray-bluish regions in Fig. 2, E to H, at the same latitude (yellow arrows in Fig. 2, B and F) and are usually interpreted as "holes" in the cloud deck. These radio-bright, dark-gray-bluish regions are most likely related 5-μm hot spots (*3*, *10*, *11*).

All of these radio-bright bands are also visible at 4 to 8 GHz, although those at 40° to 60°S just barely. The radio-hot belt at ~8°N shows less detailed structure overall than at 8 to 12 GHz, despite the higher spatial resolution in this band. To determine how deep the low NH_3 concentration in this radio-hot belt extends, we made longitude-smeared and longitude-resolved maps integrated over 1-GHz-wide frequency bands (Table 1), and we modeled these maps with radiative transfer (RT) calculations (*5*, *6*, *12*). In our calculations, we assume that the NH_3 concentration (mole fraction) is equal to 5.7×10^{-4} at $P > 8$ bar, the average value detected by the Galileo probe at these depths (*1*), which is enhanced by a factor of ~4.5 over the solar N/H ratio (*13*). We assume that all constituents (C, S, N, and O) are enhanced by this same factor. Ammonia vertical profiles in Fig. 3A include an equilibrium case (profile a), where ammonia gas is decreased at higher altitudes due to solution in the water cloud (~7.3 bar), the formation of the NH_4SH cloud (~2.5 bar), and the NH_3 ice cloud (~0.8 bar). NH_3 follows the saturated vapor pressure curve within and above the NH_3 ice cloud. Several other NH_3 profiles used in our calculations (Fig. 3, B to F) are indicated. For simplicity, we adopt step functions at different altitudes, as shown. For some profiles we adopted a relative humidity (RH) of ~1 to 10% above the NH_3 ice cloud. All model atmospheres have a temperature of 165 K at 1 bar to match the Voyager radio occultation profile (*14*). By changing the NH_3 profile, the contribution functions in an atmosphere may change substantially (Fig. 1), which helps to understand differences in the model spectra.

Figure 3B shows spectra of the NEB, at the location of the longitude-smeared radio-hot belt (peak NEB values from fig. S3), and the EZ (minimum values) (*5*), with several models based on the profiles in Fig. 3A superimposed. Clearly, the radio-hot belt is well matched by profile e: NH_3 is depleted with respect to the deeper atmosphere by a factor of 5 to 6 down to $P \sim 8$ bar, or likely deeper as shown by profile e′. In contrast, the EZ is consistent with profile a, contradicting prior analyses that the EZ is depleted in

[1]Department of Astronomy, 501 Campbell Hall, University of California, Berkeley, CA 94720, USA. [2]Faculty of Aerospace Engineering, Delft University of Technology, 2629 HS Delft, Netherlands. [3]SRON Netherlands Institute for Space Research, 3584 CA Utrecht, Netherlands. [4]School of Physics, University of Melbourne, Victoria 3010, Australia. [5]National Radio Astronomy Observatory, Socorro, NM 87801, USA.
*Corresponding author. Email: imke@berkeley.edu

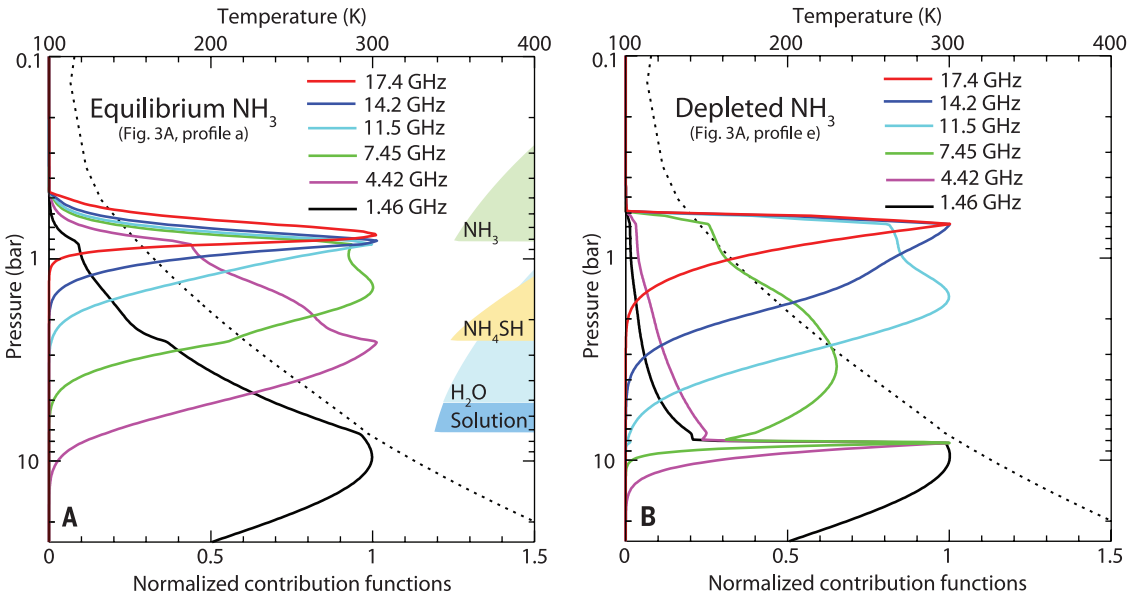

Fig. 1. Contribution functions. (**A** and **B**) Normalized contribution functions are shown for two different NH_3 profiles, as marked. The dotted line is the temperature-pressure curve in Jupiter's atmosphere. Cloud layers that are expected to form under chemical equilibrium are indicated as shaded regions in (A) (*7*).

NH_3 above the ~4-bar level (*2*). The advance in our understanding is due to the upgrade in VLA sensitivity (*15*), higher spatial resolution in longitude-averaged images than obtained previously (*2*, *6*), and full coverage over the entire 4- to 18-GHz frequency range.

The radio-hot belt contains numerous hot spots that contribute to the average NEB value. Spectra of these (at ~10°N; Fig. 3C) were extracted from 1-GHz-wide longitude-resolved maps, where maxima in T_b were recorded. We determined values for four different hot spots on each day and averaged these. The true T_b may be slightly higher, because our maps do not resolve structure within the hot spots. A comparison with models shows that hot spots are characterized by a low NH_3 concentration, less than ~10^{-4} over the 1- to 8-bar pressure level (profile e). A reasonable match to the data is given by profile f, with a concentration ~10^{-5} at the highest altitudes (P < 1 bar), gradually increasing at deeper levels.

Just south of the radio-hot belt, striking oval-shaped dark regions are visible at 4 to 8 GHz (Fig. 2D); these are also quite prominent at 8 to 12 GHz (Fig. 2C) and only barely visible at higher frequencies (Fig. 2, A and B). Spectra of these regions (~4°N), referred to as plumes, are shown in Fig. 3D. A comparison with models shows that the plumes bring NH_3 gas from deep (P > 8 bar) atmospheric levels where the ammonia concentration is 5.7×10^{-4}, up to high altitudes (P ~ 1.5 bar), contrary to previous findings that there are no locations where the full deep NH_3 concentration is brought up to the 2-bar level (*4*). A two-layer circulation pattern with thunderstorm-dominated upwelling (*4*) is therefore inconsistent with NH_3 concentrations in equatorial regions.

These plumes (Fig. 2, C and D) display a regular wave pattern with wavelength 30° and are most pronounced over a 180° range in longitude.

Table 1. VLA data and products. Column 1: Observations were conducted: A configuration: 2014/05/04; B configuration: 2013/12/23 and 2014/01/09; C configuration: 2014/12/27; D configuration: 2014/08/16. Column 2: VLA frequency band. Column 3: Center frequency of each 1-GHz-wide map. Column 4: Jupiter's effective equatorial radius (R_{eff}) for the data from the combined arrays. The C-band longitude-resolved map was constructed from only A-configuration data, with R_{eff} = 17.487″. Column 5: Disk-averaged T_b (final value) (*5*). Columns 6 and 7: Resolution or beam size (HPBW, full width at half power) in the final longitude-smeared images. Column 8: HPBW near the center of the disk in the final longitude-resolved images. 1° in latitude or longitude at Jupiter's disk center corresponds to ~1200 km.

VLA array configuration	Band	Frequency (GHz)	R_{eff} (″)	T_b (K)	HPBW (″)	HPBW (km)	HPBW (km)
B+D	Ku	13.18	15.80	159.5 ± 4.8	0.25	1130	~1550
B+D	Ku	14.21	15.80	154.5 ± 4.6	0.25	1130	~1450
B+D	Ku	15.18	15.80	150.6 ± 4.5	0.25	1130	~1300
B+D	Ku	16.21	15.80	146.4 ± 4.4	0.25	1130	~1250
B+D	Ku	17.38	15.80	143.5 ± 4.3	0.25	1130	~1180
B+C	X	8.50	21.46	187.7 ± 5.7	0.35	1166	~2300
B+C	X	9.52	21.46	177.5 ± 5.4	0.35	1166	~2100
B+C	X	10.46	21.46	172.4 ± 5.2	0.35	1166	~2000
B+C	X	11.46	21.46	165.8 ± 5.0	0.35	1166	~1750
A+C	C	4.52	21.46	247.5 ± 7.4	0.25	833	~1275
A+C	C	5.49	21.46	223.3 ± 6.7	0.25	833	~1100
A+C	C	6.50	21.46	207.6 ± 6.2	0.25	833	~980
A+C	C	7.50	21.46	192.9 ± 5.8	0.25	833	~900

A comparison of the location of five plumes on the 8- to 12-GHz map on 23 December 2013 (indicated by red arrows in Fig. 2C) with that on 9 January 2014 (*5*) reveals an eastward phase velocity of 102.2 ± 1.4 m/s relative to the System III coordinate system, which is ~20 to 25% slower than the 7.8°N eastward jet at 130 m/s (*16*). These characteristics are very similar to those displayed by 5-μm hot spots (*17*). These plumes could be the deep signature of the equatorially trapped Rossby wave thought to be responsible for forming the 5-μm hot spots. Numerical simulations of such Rossby waves showed regions with a high NH_3 concentration in between (and slightly south of) the simulated hot spots (*10*, *11*). At higher altitudes, the ammonia gas in these plumes will condense out, and as such could be responsible for the spectroscopically identified fresh ammonia ice clouds detected by the Galileo spacecraft at these latitudes (*18*).

Other prominent features in the radio maps are anticyclones, in particular the Great Red Spot (GRS)

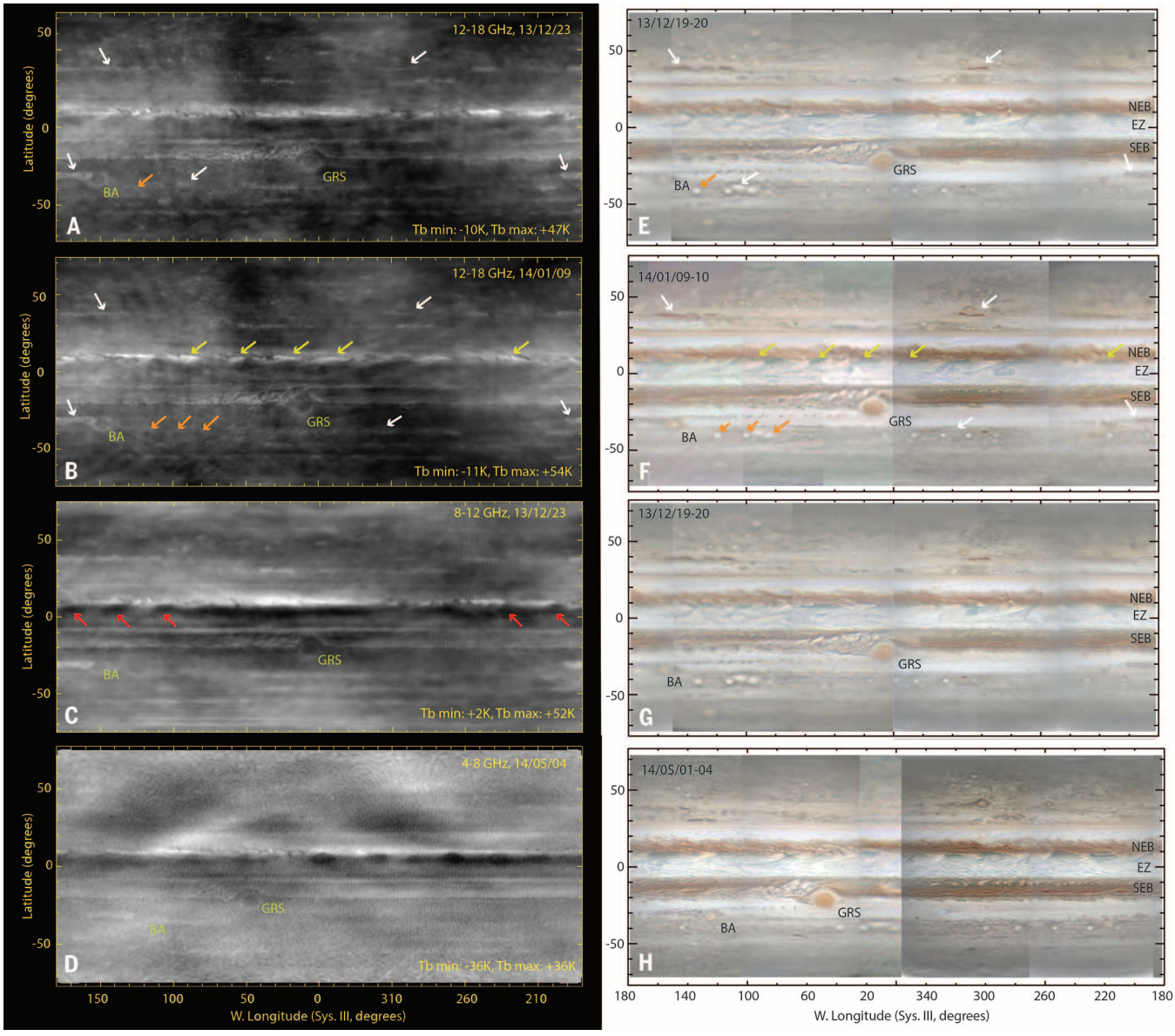

Fig. 2. Longitude-resolved VLA maps of Jupiter. (**A** to **D**) Longitude-resolved radio maps of Jupiter, after subtraction of a uniform limb-darkened disk (*5*). Each map has been integrated over the full ~4- to 6-GHz bandwidth. (**E** to **H**) Visible-light maps taken close in time with the VLA maps, as compiled by the amateur community (*8*). The axes indicate west longitude (in System III, prime meridian rotation angle of the magnetic field) and planetographic latitude. In addition to the GRS and Oval BA, several features discussed in the text are highlighted by arrows on both a 12- to 18-GHz and visible wavelength map. The red arrows in Fig. 2C indicate the plumes used to derive their phase velocity through comparison with the 8- to 12-GHz map from 9 January 2014 (*5*). T_b min and T_b max give the differences in temperature for the minimum and maximum observed deviations from zero (i.e., with respect to the uniform limb-darkened disk that was subtracted).

and Oval BA but also the series of white ovals at 40°S (orange arrows) and numerous other small ovals. Anticyclones look relatively dark, often surrounded by a radio-bright ring, in contrast to cyclonic features, which are radio-bright (white arrows). These features are most apparent in the 8- to 12- and 12- to 18-GHz maps (i.e., at pressure levels <2 to 3 bar) (Fig. 1). The GRS is partially embedded in the SEB, which is relatively quiescent east of the GRS and extremely turbulent to the northwest. This turbulence produces the same fine-scale inhomogeneity in the radio maps as well as the visible clouds. Oval BA is also characterized by a turbulent, relatively radio-bright, region to the west (resembling a cyclonic feature) and a quiescent region to the east. Figure 3, E to F, shows spectra of the GRS and Oval BA. The NH_3 concentration over the GRS itself looks similar to that of the EZ, except that it is depleted by a factor of ~2 down to ~1.5 bar (profile b) as compared to the EZ. The NH_3 concentration in the bright ring is depleted twice as much, down to ~2 to 2.5 bar (profile d). Although one would expect Oval BA and the GRS to have similar NH_3 profiles, given their similar secondary circulation and sensitivity to environmental stratification (*19*), the VLA spectra reveal differences that might be related to entrainment from surrounding belts and zones with different NH_3 concentrations.

Our VLA maps at 8 to 18 GHz reveal structure at every resolvable length scale, tracing dynamical flows primarily at pressures $\lesssim$2 to 3 bar, where ammonia is strongly modulated by cloud condensation. At all observed frequencies, we find a radio-hot belt near the 7.8°N eastward jet, which

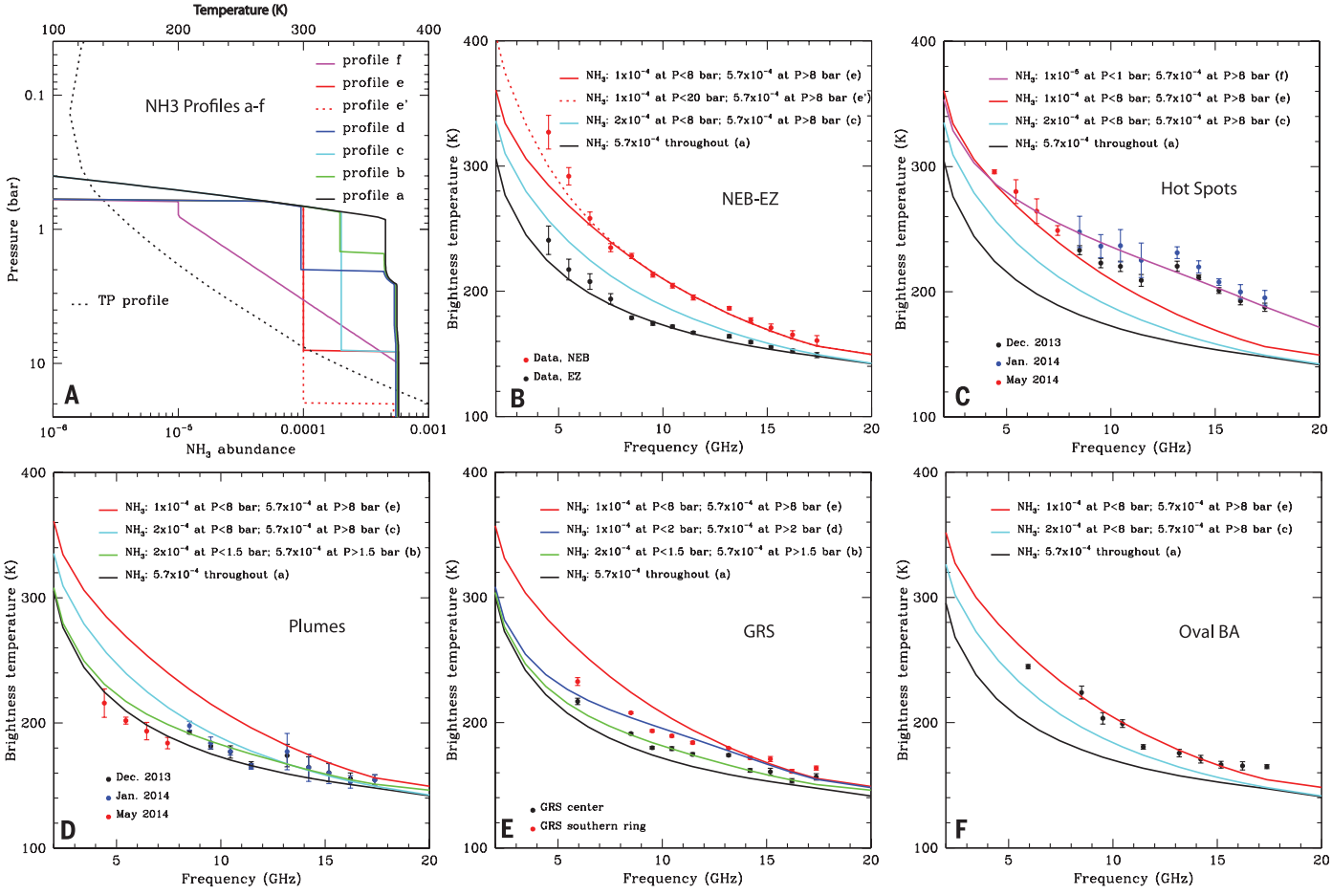

Fig. 3. Frequency dependence of specific features. (**A**) Altitude profiles of the NH_3 concentration used in the various models. The black-dotted line shows the temperature-pressure profile. Profile a follows the saturated vapor pressure curve for NH_3 within and above the NH_3 ice cloud (RH = 100%), whereas for the horizontal lines at a pressure of 0.6 bar, RH = 1%. (**B**) Longitude-averaged brightness temperature as a function of frequency for the NEB and EZ, with RT models superimposed; T_b maxima (NEB) and minima (EZ) from fig. S3 are plotted (*5*). Error bars are the standard deviation along the constant-latitude line. (**C** to **F**) T_b versus frequency for the GRS, Oval BA, hot spots, and plumes. Models are superimposed. The T_b for the GRS, Oval BA, and four plumes are averaged over the central regions; the values for the four plumes were averaged. The error bars give the standard deviation. The T_b for hot spots are local maxima; the error bars indicate the spread in the measured T_b.

contains the radio counterpart of the 5-μm hot spots, characterized by a low NH_3 concentration down to ~8 bar. The ascending branch of the equatorially trapped Rossby wave that produces the 5-μm hot spots carries the deep atmospheric NH_3 concentration up to the visible cloud layers, producing dark plumes in the VLA maps.

REFERENCES AND NOTES

1. M. H. Wong, P. R. Mahaffy, S. K. Atreya, H. B. Niemann, T. C. Owen, *Icarus* **171**, 153–170 (2004).
2. I. de Pater, D. Dunn, K. Zahnle, P. N. Romani, *Icarus* **149**, 66–78 (2001).
3. R. J. Sault, C. Engel, I. de Pater, *Icarus* **168**, 336–343 (2004).
4. A. P. Showman, I. de Pater, *Icarus* **174**, 192–204 (2005).
5. See the supplementary materials.
6. I. de Pater, D. DeBoer, M. Marley, R. Freedman, R. Young, *Icarus* **173**, 425–438 (2005).
7. M. H. Wong, S. K. Atreya, W. R. Kuhn, P. N. Romani, K. M. Mihalka, *Icarus* **245**, 273–281 (2015).
8. Marco Vedovato constructed groundbased optical Jupiter maps (from images taken by Christopher Go, Tadashi Horiuchi, Michel Jacquesson, Manos Kardasis, John Rozakis, Ian Sharp, Joost Verheyden, and Sean Walker) using Grischa Hahn's WinJupos software, available from http://jupos.org.
9. J. J. Lissauer, I. de Pater, *Fundamental Planetary Science* (Cambridge Univ. Press) (2013).
10. A. J. Friedson, *Icarus* **177**, 1–17 (2005).
11. A. P. Showman, T. E. Dowling, *Science* **289**, 1737–1740 (2000).
12. I. de Pater *et al.*, *Icarus* **237**, 211–238 (2014).
13. M. Asplund, N. Grevesse, A. J. Sauval, P. Scott, *Annu. Rev. Astron. Astrophys.* **47**, 481–522 (2009).
14. G. F. Lindal, *Astron. J.* **103**, 967–982 (1992).
15. R. A. Perley, C. J. Chandler, B. J. Butler, J. M. Wrobel, *Astrophys. J.* **739**, L1 (2011).
16. X. S. Asay-Davis, P. S. Marcus, M. H. Wong, I. de Pater, *Icarus* **211**, 1215–1232 (2011).
17. J. L. Ortiz *et al.*, *J. Geophys. Res.* **103**, 23051–23069 (1998).
18. K. H. Baines, R. W. Carlson, L. W. Kamp, *Icarus* **159**, 74–94 (2002).
19. M. H. Wong, I. de Pater, X. Asay-Davis, P. S. Marcus, C. Y. Go, *Icarus* **215**, 211–225 (2011).

ACKNOWLEDGMENTS

This research was supported by NASA Planetary Astronomy (PAST) award NNX14AJ43G and NASA Outer Planets Research Program award NNX11AM55G. The National Radio Astronomy Observatory (NRAO) is a facility of NSF operated under cooperative agreement by Associated Universities, Inc. VLA data used in this report, associated with project code 13B-064, are available from the NRAO Science Data Archive at https://archive.nrao.edu/archive/advquery.jsp. Ground-based optical Jupiter maps (*8*) are available from the Planetary Virtual Observatory & Laboratory (PVOL) website at http://www.pvol.ehu.es/pvol/index.jsp?action=iopw. We thank three anonymous reviewers for their thoughtful comments on this paper.

SUPPLEMENTARY MATERIALS

www.sciencemag.org/content/352/6290/1198/suppl/DC1
Materials and Methods
Figs. S1 to S5
Tables S1 and S2
References (*20–26*)

8 January 2016; accepted 29 April 2016
10.1126/science.aaf2210

www.sciencemag.org/content/352/6290/1198/suppl/DC1

Supplementary Materials for

Peering through Jupiter's clouds with radio spectral imaging

Imke de Pater,* R. J. Sault, Bryan Butler, David DeBoer, Michael H. Wong

*Corresponding author. Email: imke@berkeley.edu

Published 3 June 2016, *Science* **352**, 1198 (2016)
DOI: 10.1126/science.aaf2210

This PDF file includes:

1. Observations and Data Reduction

Radio observations of Jupiter were conducted with the upgraded Very Large Array (VLA) *(15)*. We observed Jupiter for 10 hrs on each of 4 days, each day with a different array configuration. In the A configuration, the antennas have a maximum separation of 36 km, with a minimum spacing of 0.68 km. In contrast, in the most compact or D configuration, the longest spacing between antennas is 1 km, and the shortest spacing is 0.035 km. The B configuration has spacings between 0.21 km and 11.1 km, and the C configuration between 0.035 km and 3.4 km. By carefully choosing our configurations and frequencies we were able to cover Jupiter at all frequencies with both long and short spacings, as summarized in Table S1.

Observations in the Ku (12-18 GHz), X (8-12 GHz), and C (4-8 GHz) bands are reported. The flux density scale was calibrated using 3C286, with the standard VLA flux calibrator scale *(20)*. Internal and absolute uncertainties in the flux densities are believed to be better than 3% at 4–18 GHz, although there appeared to be a one-time flux calibration error of 6.5% in the X and C band data from December 2014, as discussed below.

The initial processing of the data, such as flagging/editing and calibration, was done via the internal VLA calibration pipeline. All subsequent data reduction (and in some cases the entire data reduction process) was performed using the MIRIAD software package *(21)*. Each dataset was inspected for interfering background sources; none were found in these particular datasets. Two sources which did interfere with the data were the satellites Io and Europa. By phase shifting the u-v data such as to follow the motion of these satellites, their contribution was subtracted from the u-v data. In the end the u-v data were phase shifted back to follow the motion of Jupiter on the sky. These data sets were then split into roughly 1-GHz wide datasets (Table S2), each of which was processed independently.

For each of these data sets, a sequence of imaging and self-calibration cycles was performed. Self-calibration uses a model of the visibilities to derive antenna-based corrections to the visibilities so that the visibilities over time are self-consistent in the end. Each self-calibration and imaging step is based on a model of the visibilities that is based on the last image that was created from the self-calibrated data. Although in principle both the amplitude and phase can be corrected this way, we only corrected the phase of the visibilities. This sequence of self-calibration and imaging proceeded until the image quality was maximized.

In order to best assess small variations on Jupiter's disk, a limb-darkened disk was subtracted from the u-v data with a brightness temperature and limb-darkening parameter that produced a best fit to the data. Limb-darkening was modeled by multiplying the brightness temperature T_b by $(\cos\ )^q$, with the emission angle on the disk (i.e., the angle a ray makes with the line-of-sight to Earth), and q a constant that provides a best fit to the data. Since we had split the data into 1-GHz wide chunks, we could match the data reasonably well with these parameters, but not perfectly. In many cases a bright ellipse was left on the limb of the planet after subtraction of a limb-darkened disk. To minimize this effect, we scaled the size of the planet that was subtracted by a small scaling factor, listed in Table S2. Longitude-smeared maps of each 1-GHz wide dataset were then produced. The data from the most widely spaced configurations, i.e., the X and Ku band in the B configuration and the C band in the A configuration, best show the latitudinal variations across the disk. However, these data also suffer from a lack of short spacing data, visible as a negative bowl underlying the disk *(2)*, so that the absolute brightness temperature cannot be determined. The data from the more compact arrays have too poor a spatial resolution to be useful for any analysis of brightness variations across the disk. However, these data can fill in the missing short spacings of the A and B configurations. In order not to add in data from the C and D configurations that resolve the disk, we only added spacings smaller than 12 k (is wavelength) to the extended arrays.

2. Longitude-smeared Results

Figure S1 shows the longitude-smeared images in each of the Ku, X, and C bands (i.e., averaged in frequency over each band), after subtraction of a uniform limb-darkened disk from each of the 1-GHz-wide datasets with brightness temperatures and limb-darkening parameters as summarized in Table S2. Since images from the individual observing sessions in December 2013 and January 2014 did not show changes in the location of the zones and belts, we combined all B configuration Ku and X band data to construct these images. For C-band, we used observations taken in the A configuration in May 2014. As discussed above, we combined these data with the short spacing ($<$ 12 k) data from observations taken in the D configuration (Ku band: August 2014) and the C configuration (X and C band: December 2014).

In order to compare our data with previous disk-averaged brightness temperatures, we determined the disk-averaged brightness temperature of Jupiter for each of the 1-GHz chunks of u-v data, i.e., consisting both of the disk-averaged brightness temperature, T_b(av), of the best-fit uniform limb-darkened disk (with center value T_b), and the residual brightness in the

longitude-smeared maps (mainly due to the zone-belt structure), T_{res}. These numbers are listed in Table S2. Since Jupiter blocks the cosmic microwave background, we determined this brightness temperature, T_{cmb}, at each frequency *(22)*, and added these numbers to the observed temperatures. Figure S2 shows these values (red dots at Ku band; red open circles at X and C band) together with disk-averaged brightness temperatures obtained over the years by others, as listed in the figure caption. The sequence of open red circles is clearly disjoint from the solid red dots at Ku band, and are suggestive of a calibration error. By multiplying all X and C band data by a factor of 1.065, the red open circles are shifted upwards to match the solid red dots at Ku band.

Finally, the C and X band data are partially contaminated by Jupiter's synchrotron radiation. From spatially-resolved models of Jupiter's synchrotron radiation *(25)*, we estimated the contamination on the disk to be roughly 6-7% of the total synchrotron radiation. By using spectra of the total synchrotron radiation *(26)*, we determined the contaminating flux density at each fequency; after conversion to a disk-averaged value, T_{synch}, we subtracted it from the disk-averaged brightness temperatures T_b(av). The final values $T_b(\text{final}) = factor*(T_b(\text{av})+T_{res})+T_{cmb}-T_{synch}$ ($factor = 1$ at Ku band, $factor = 1.065$ at X and C band) are listed in Table S2. We adopted a 3% error on the measurements. These numbers are plotted as solid red dots in Fig. S2.

Figure S3 shows north-south scans through the 1-GHz wide longitude-smeared maps (i.e., images as shown in Fig. S1, but for each 1-GHz wide dataset; the 1-GHz images look very similar to those shown in Fig. S1). These scans were constructed by median averaging over 80 of longitude, centered on the central meridian, after deprojecting the images. Since a uniform limb-darkened disk had been subtracted from the images, fine-scale structure is easily discerned. We then determined the maximum values in the NEB and minimum values of the EZ from the north-south scans, and plotted these in Fig. 3B. The error bars in Fig. 3B represent the standard deviation along the latitudes at the NEB and EZ.

3. Radiative Transfer (RT) Calculations

We model our data with a radiative transfer (RT) code *(6,12)*. We assume the atmosphere to be in thermochemical equilibrium, and calculate the atmospheric structure after specification of the temperature, pressure, and composition of one mole of gas at some deep level in the atmosphere, well below the condensation level of the deepest cloud layer (typically a few 10,000 bar). The model then steps up in altitude, in roughly 1 km steps. At each level, the new temperature is calculated assuming an adiabatic lapse rate, and the new pressure by using hydrostatic equilibrium. The partial pressures of each trace gas in the

atmosphere is computed. In our RT code, the criterion for a trace gas to condense and for a cloud to form from the condensate is that the partial pressure of the trace gas exceeds its saturation vapor pressure, or equivalently, that the temperature be below the "dew point" of the trace gas.

In Jupiter's atmosphere we expect an aqueous ammonia solution cloud (H_2O-NH_3-H_2S), water ice, ammonium hydrosulfide (NH_4SH) solid, and ammonia ice, as indicated in Fig. 1. Since the NH_4SH cloud forms as a result of a reaction between NH_3 and H_2S gases, the test for NH_4SH cloud formation is that the equilibrium constant of the reaction is exceeded. Both NH_3 and H_2S are reduced in equal molar quantities until the product of their atmospheric pressures equals the equilibrium constant. As the trace gases are removed from the atmosphere by condensation, "dry" air (an H_2-He mixture) is entrained into the parcel to ensure the mixing ratios add up to one. This cycle is repeated until the tropopause temperature is reached. We choose the temperature and pressure at our base level such that for every model the temperature is close to 165 K at the 1 bar level to match the Voyager radio occultation profile *(14)*. The temperature profile is shown in Figure 1.

Cloud densities are computed analogously to adiabatic liquid water contents for terrestrial clouds, i.e., they represent maximum cloud densities based on assuming no loss by precipitation. By including dynamics, such as in updrafts, cloud densities may be orders of magnitude lower than those calculated via equilibrium models *(7)*. We therefore decided to ignore the direct effect of cloud opacity on the microwave spectrum, and include only the gas opacity.

The gas opacity in Jupiter's atmosphere is primarily determined by collision-induced absorption due to hydrogen gas (CIA: we include H_2-H_2, H_2-He, H_2-CH_4), NH_3 and some H_2S, while at longer wavelengths H_2O becomes noticeable; at the frequencies used to observe Jupiter in this paper, ammonia gas is the dominant source of opacity *(2,6)*.

We superpose several models on the disk-averaged brightness temperature data in Fig. S2: the blue line is for an atmosphere with C, N, O, and S abundances according to the most recent estimates for the proto-solar nebula *(13)*: $C/H_2 = 5.90 \times 10^{-4}$; $N/H_2 = 1.48 \times 10^{-4}$; $O/H_2 = 1.07 \times 10^{-3}$; $S/H_2 = 2.89 \times 10^{-5}$; $Ar/H_2 = 5.50 \times 10^{-6}$. The cyan line is for an atmosphere in which all above elements were enhanced by a factor of 4.5 over the proto-solar values, providing an NH_3 abundance (i.e., volume density) in the deep atmosphere of 5.74×10^{-4} (Profile a in Fig. 3A). At higher altitudes this number decreases due to cloud formation. We assumed a 100% relative humidity, i.e., a fully saturated profile. The red line is for an atmosphere with an NH_3 abundance equal to 2.0×10^{-4} at $P < 8$ bar, and 5.7×10^{-4} at $P > 8$ bar; NH_3 is assumed to be fully saturated (Profile c in Fig. 3A). The dashed red line has a 10% relative humidity, which shifts the line upwards near 1.3 cm *(22)*.

4. Longitude-resolved Maps

The longitude-smeared radio maps discussed above are what we refer to as "conventional radio interferometric images", which usually are integrated over many hours to meet the required sensitivity, while Earth rotation synthesis helps to achieve good sampling of the Fourier plane. Consequently, imaging planets in this conventional way smears any structure in longitude because of the rotation of the planet. In principle one can merge together snapshots of the same rotational aspect of the planet from observations taken on different days, if the structure does not change over time. To image Jupiter's thermal radiation on length-scales of interest in the atmosphere, one requires a high spatial resolution, ideally 0.5-1 . In 5 minutes of time, the rotational smearing at the disk center is 1 , and hence integration times should be of order 1 minute or less. Such images would have such poor signal-to-noise ratio (SNR) that even the zones and belts on Jupiter may not be recognized.

To overcome these problems, we developed an innovative technique to synthesize together many hours of radio data such that a longitude-resolved map can be produced *(3)*. This method works best at wavelengths < 4 cm, where the influence of Jupiter's synchrotron radiation is very small. At longer wavelengths Jupiter's flux density becomes increasingly more dominated by the planet's nonthermal radiation (e.g., C band image in Fig. S1). We used this technique to create longitude-resolved maps of Jupiter's thermal emission for each 1-GHz-wide u-v dataset, and also by combining all u-v data in each of the three bands. For the X and Ku band maps we used the combination of the extended arrays and the short spacing data up to 12 k from the compact arrays (Table S2); for the C band data, the synchrotron radiation from the short spacing data contaminated the map too much. However, using only the A array data where the synchrotron radiation is effectively resolved out, we were able to construct reliable maps. The brightness temperatures for individual features, when plotted with those at Ku and X bands, suggest that these data do not suffer too much from the missing short spacing problem. This can be partially explained by the fact that a limb-darkened disk with the "proper" disk parameters (Table S2) was subtracted, followed by a cleaning process which technically should result in a proper absolutely calibrated map. This process was iterated with several self-calibration cycles (see Section 1 above).

The above mapping technique results in a resolution that varies across Jupiter's disk, and with frequency. Examples of the beam patterns are shown in Fig. S4 for the Ku, X, and C bands, for the jovian radio maps in Fig. 2. Figure S5 shows the longitude-resolved map at X band (8-12 GHz) from 2014 January 9. We used this map, together with the 8-12 GHz map from 2013 December 23 to derive the phase velocity of five cold plumes (indicated by red arrows).

Table S1: VLA Observations

Date (UT) year/month/day	VLA Array configuration	Band	Frequency range (GHz)	(AU)	R (equ) ( )	R (pol) ( )	Obs-lat ( )
2013/12/23	B	Ku	12-18	4.236	23.272	21.762	1.85
2013/12/23	B	X	8-12	4.236	23.272	21.762	1.85
2014/01/09	B	Ku	12-18	4.214	23.394	21.877	1.87
2014/01/09	B	X	8-12	4.214	23.394	21.877	1.87
2014/05/04	A	C	4-8	5.637	17.487	16.353	1.35
2014/08/16	D	Ku	12-18	6.237	15.803	14.778	0.82
2014/12/27	C	X	8-12	4.594	21.458	20.066	-0.26
2014/12/27	C	C	4-8	4.594	21.458	20.066	-0.26

=geocentric distance, R = radius (equator and polar), and Obs-lat is the observer's (or sub-) latitude.

Table S2: Details on the VLA maps

Array configuration	Band	Center Frequ (GHz)	R_{eff} ( )	T_b (K)	q	scaling	T_b(av) (K)	T_{res} (K)	T_{cmb} (K)	T_{synch} (K)	T_b(final) (K)	HPBW ( )	HPBW (km)	HPBW km
B+D	Ku	13.18	15.80	161.86	0.08	1.000	153.5	3.5	2.42	0	159.5±4.8	0.25	1130	1550
B+D	Ku	14.21	15.80	158.14	0.08	1.000	150.0	2.1	2.40	0	154.5±4.6	0.25	1130	1450
B+D	Ku	15.18	15.80	154.42	0.08	1.000	146.5	1.8	2.38	0	150.6±4.5	0.25	1130	1300
B+D	Ku	16.21	15.80	150.70	0.08	1.000	143.0	1.1	2.36	0	146.4±4.4	0.25	1130	1250
B+D	Ku	17.38	15.80	146.05	0.06	1.000	139.8	1.3	2.33	0	143.5±4.3	0.25	1130	1180
B+C	X	8.50	21.46	183.0	0.16	1.0012	167.4	7.8	2.53	1.4	187.7±5.7	0.35	1166	2300
B+C	X	9.52	21.46	177.0	0.16	1.0012	161.9	3.2	2.50	0.9	177.5±5.4	0.35	1166	2100
B+C	X	10.46	21.46	171.0	0.16	1.0012	156.4	3.7	2.48	0.6	172.4±5.2	0.35	1166	2000
B+C	X	11.46	21.46	165.0	0.16	1.0012	150.9	2.8	2.46	0.3	165.8±5.0	0.35	1166	1750
A+C	C	4.52	21.46	237.0	0.16	1.001	216.8	21.8	2.62	9.2	247.5±7.4	0.25	833	1275
A+C	C	5.49	21.46	222.0	0.16	1.001	203.1	9.3	2.60	5.5	223.3±6.7	0.25	833	1100
A+C	C	6.50	21.46	209.0	0.16	1.001	191.2	4.6	2.58	3.4	207.6±6.2	0.25	833	980
A+C	C	7.50	21.46	199.0	0.16	1.001	182.0	-1.2	2.55	2.2	192.9±5.8	0.25	833	900

Column 4: Jupiter's effective equatorial radius for the data from the combined arrays. The C-band longitude-resolved map was constructed from only A array data, and R_{eff} was 17.487 .
Column 5: Brightness temperature of the uniform limb-darkened disk that gave a best fit to the data.
Column 6: Limb-darkening parameter of the best-fit uniform limb-darkened disk.
Column 7: Scaling factor of the best-fit disk.
Column 8: Disk-averaged temperature of the uniform limb-darkened disk that was subtracted.
Column 9: Residual disk-averaged brightness temperature, after subtraction of the best-fit disk (primarily due to the zone-belt structure).
Column 10: Cosmic microwave background correction, T_{cmb} *(12,22)*.
Column 11: Disk-averaged brightness temperature due to Jupiter's synchroton radiation.
Column 12: Final disk-averaged brightness temperature, where the X and C band data values (T_b(av)+T_{res}) are multiplied by an extra calibration factor, $factor = 1.065$ (see text). T_{cmb} was added, and the synchrotron radiation, T_{synch}, was subtracted: T_b(final)= $factor$*(T_b(av)+T_{res})+T_{cmb}-T_{synch} ($factor = 1$ at Ku band). We adopted a 3% calibration error.
Columns 13, 14: Resolution or beamsize (HPBW, full width at half power) in the final longitude-averaged images. 1 in latitude/longitude on Jupiter's disk corresponds to 1200 km.
Column 15: Approximate resolution or beamsize (HPBW, full width at half power) near the center of the disk in the final longitude-resolved images. 1 in latitude/longitude on Jupiter's disk corresponds to 1200 km.

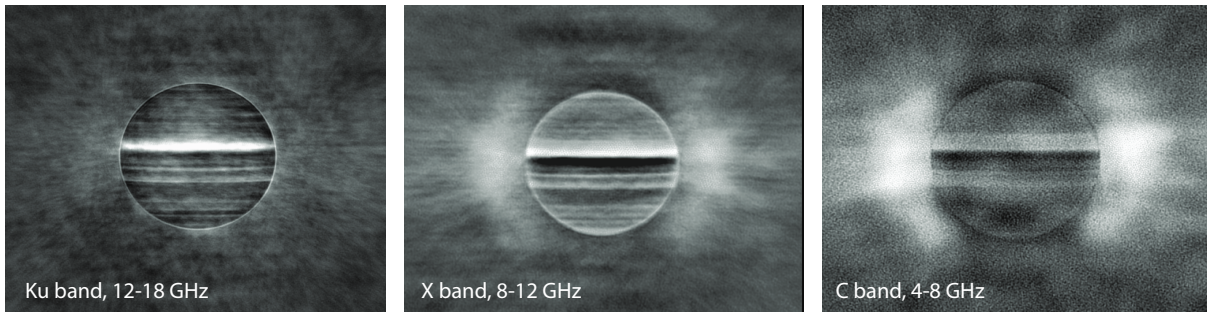

Fig. S1. Longitude-smeared images of Jupiter. Images of Jupiter are shown at Ku (12-18 GHz), X (8-12 GHz), and C (4-8 GHz) bands, after subtraction of a unifrom limb-darkened disk with parameters as given in Table S2.

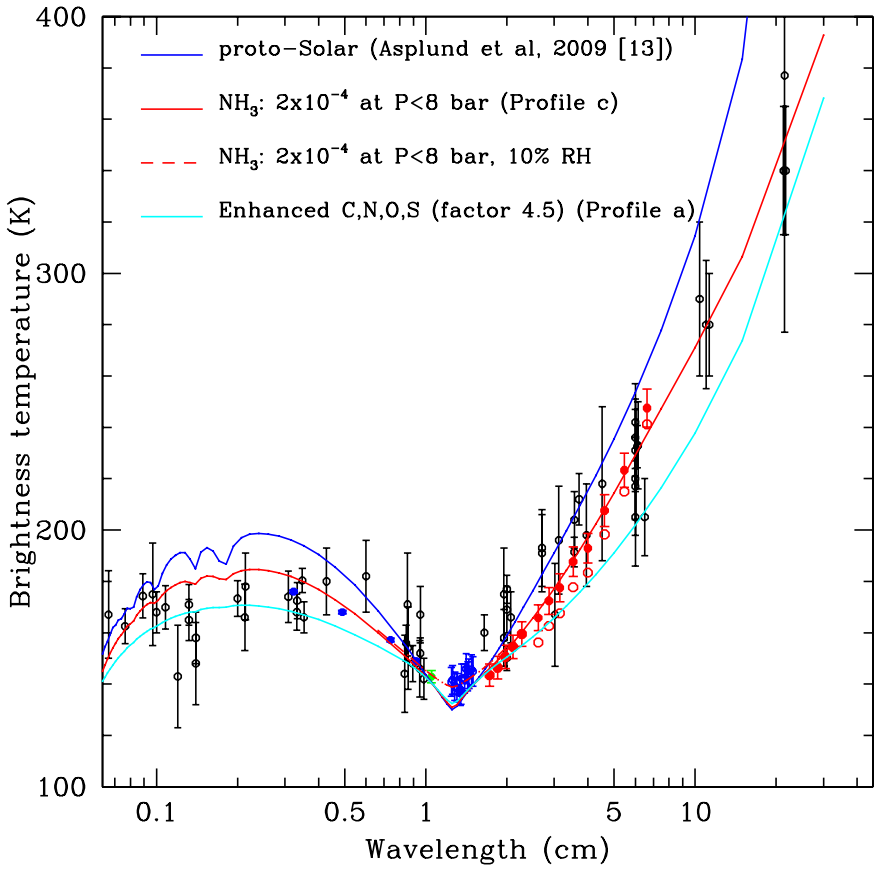

Fig. S2. Jupiter's disk-averaged brightness temperature as a function of wavelength. The filled red dots with errorbars are the values reported in this paper (Table S2). The open red circles are the values at X and C band before correcting a calibration error (see text). The black symbols are older datapoints, as compiled in *(6)*. The open blue circles near 1.3 cm *(23)*, the filled blue dots *(24)*, and the green datapoint *(22)* were corrected according to the procedures outlined in *(22)*. The various curves are model calculations, with parameters as shown on the figure. The particular model is referred to in the legend, and some of these were plotted in Fig. 3A, as indicated. All profiles have an ammonia abundance of 5.74×10^{-4} at $P > 8$ bar.

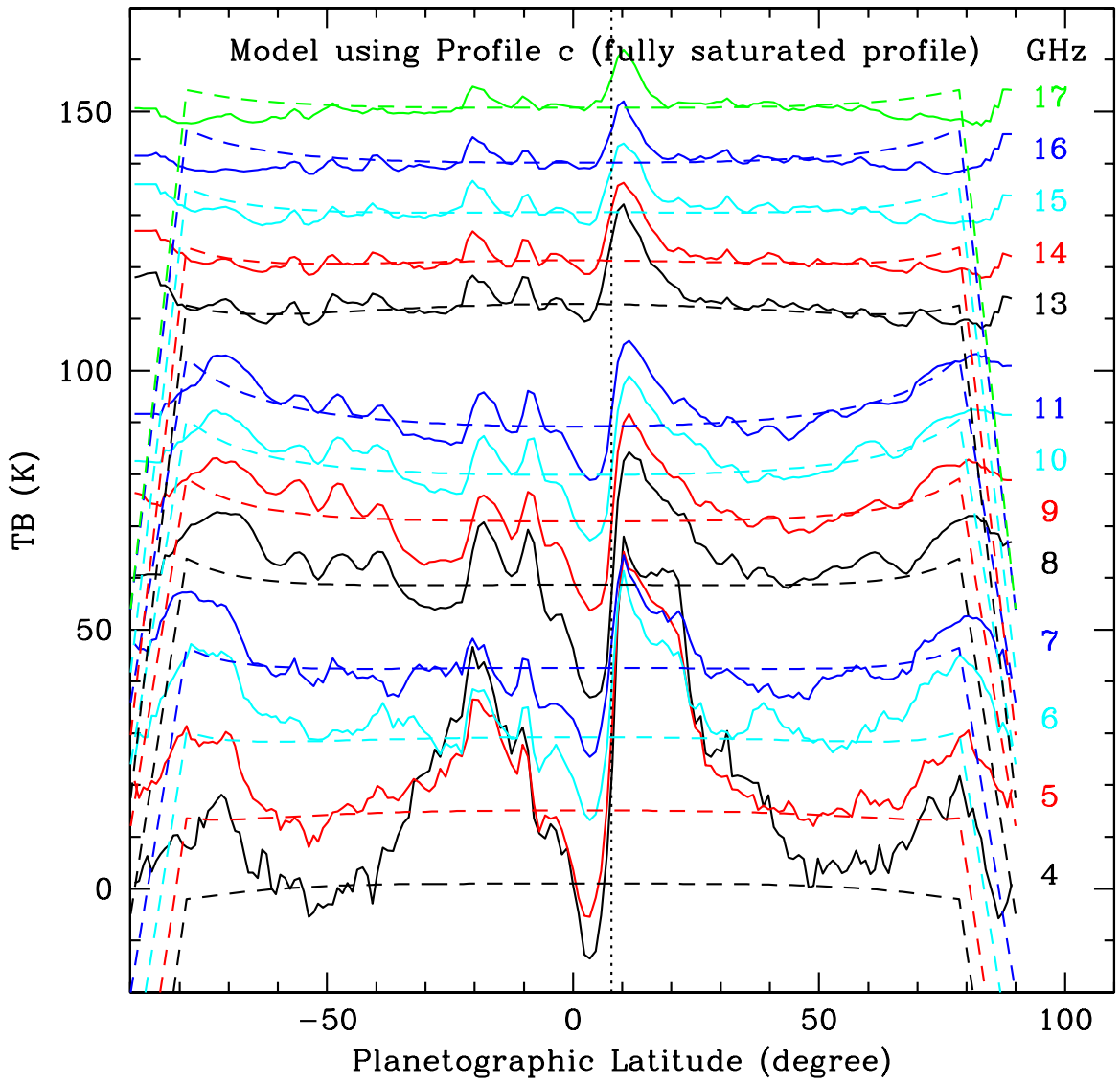

Fig. S3. North-south scans through the longitude-smeared images. North-south scans through longitude-smeared images (as displayed in Fig. S1), by median averaging over 80 of longitude centered on the central meridian in each of the 1-GHz wide maps. Each of these maps was constructed from the combined high and low resolution data, as detailed in the text. As in Fig. S1, these scans were taken through images after subtraction of a limb-darkened disk with parameters as given in Table S2. The beamsize is also provided in Table S2. The scans are plotted as a function of planetographic latitude. The dashed lines are models that match the overall level (or "baseline") of the scans. This particular model is indicated by Profile c in Fig. 3A. The vertical dotted line is the latitude of the eastward jet at 7.8 N planetographic latitude.

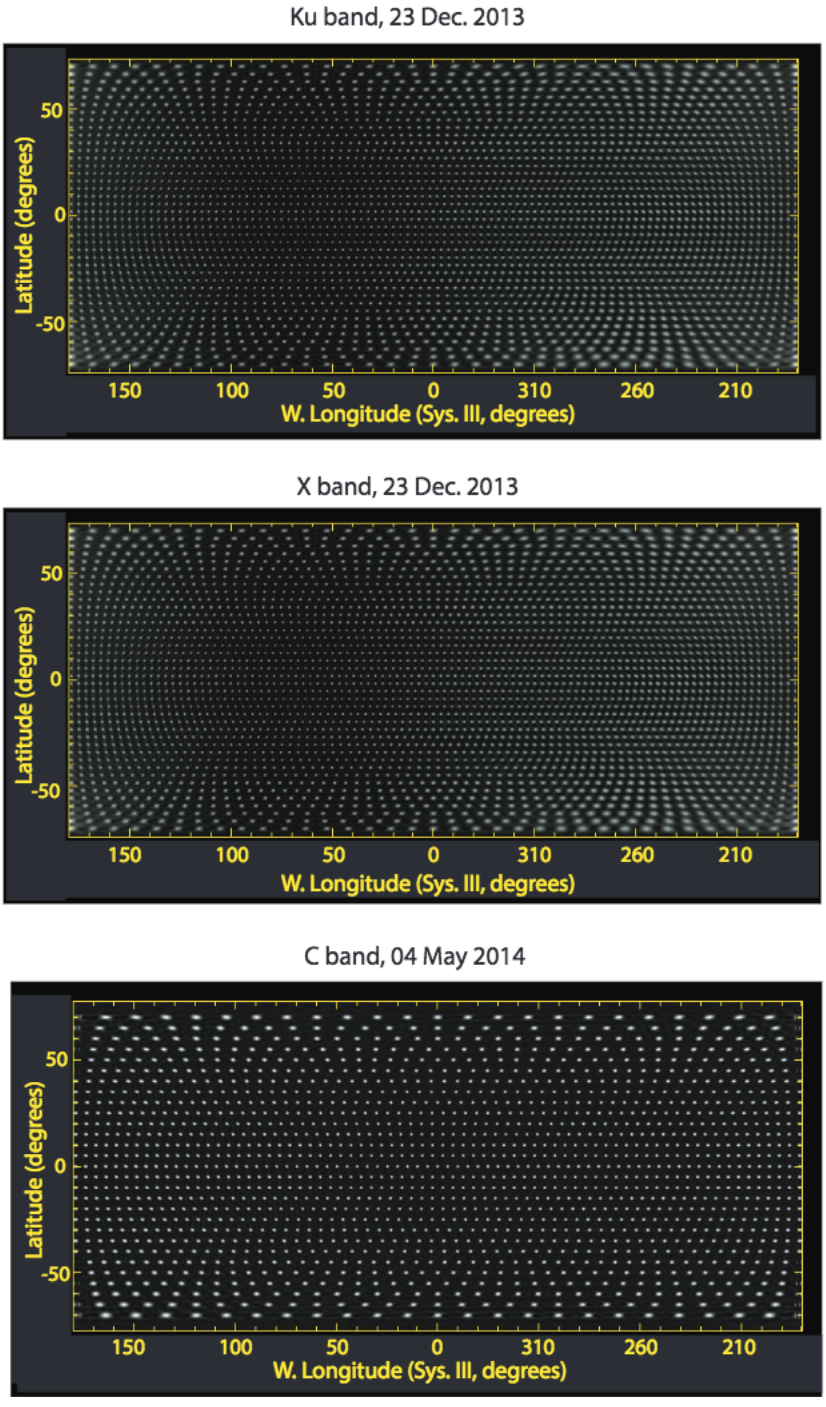

Fig. S4. **Beam patterns of the longitude-resolved maps in Fig. 2.** The resolution for the longitude-resolved maps varies from frequency-to-frequency, and across Jupiter's disk. Each feature in these images corresponds to the beam pattern at that particular location on Jupiter in the various bands, for the images shown in Fig. 2.

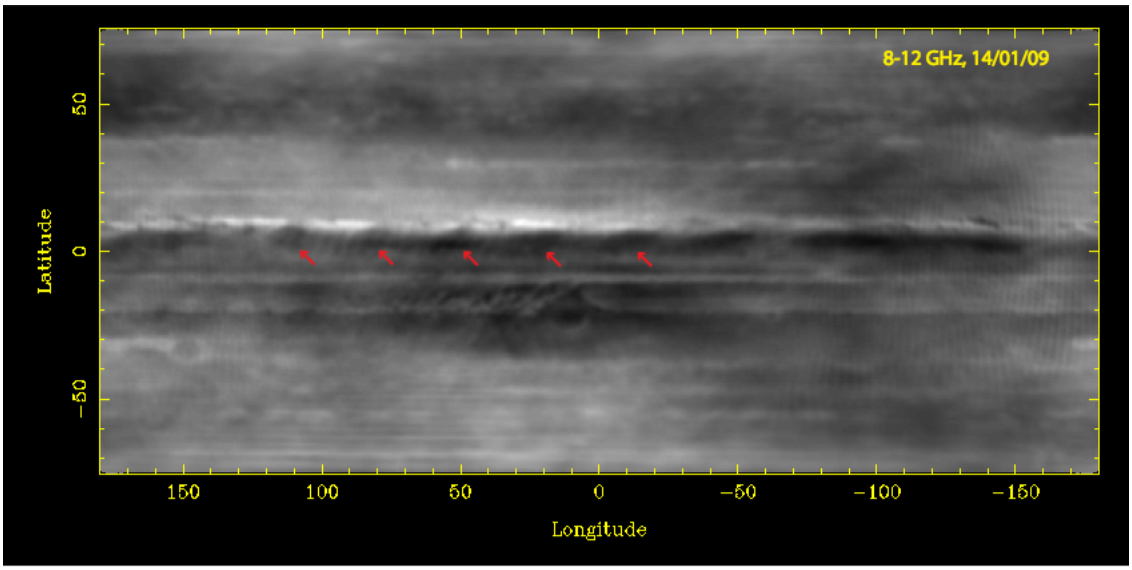

Fig. S5. Longitude-resolved map at 8-12 GHz from 2013 December 23. The red arrows indicate the cold plumes that were used together with those in Fig. 2C to derive the phase velocity of these plumes.

REFERENCES AND NOTES

1. M. H. Wong, P. R. Mahaffy, S. K. Atreya, H. B. Niemann, T. C. Owen, Updated Galileo probe mass spectrometer measurements of carbon, oxygen, nitrogen, and sulfur on Jupiter. *Icarus* **171**, 153–170 (2004). doi:10.1016/j.icarus.2004.04.010

2. I. de Pater, D. Dunn, K. Zahnle, P. N. Romani, Comparison of Galileo probe data with ground- based radio measurements. *Icarus* **149**, 66–78 (2001). doi:10.1006/icar.2000.6527

3. R. J. Sault, C. Engel, I. de Pater, Longitude-resolved imaging of Jupiter at $\lambda = 2$ cm. *Icarus* **168**, 336–343 (2004). doi:10.1016/j.icarus.2003.11.014

4. A. P. Showman, I. de Pater, Dynamical implications of Jupiter's tropospheric ammonia abundance. *Icarus* **174**, 192–204 (2005). doi:10.1016/j.icarus.2004.10.004

5. See the supplementary materials.

6. I. de Pater, D. DeBoer, M. Marley, R. Freedman, R. Young, Retrieval of water in Jupiter's deep atmosphere using microwave spectra of its brightness temperature. *Icarus* **173**, 425–438 (2005). doi:10.1016/j.icarus.2004.06.019

7. M. H. Wong, S. K. Atreya, W. R. Kuhn, P. N. Romani, K. M. Mihalka, Fresh clouds: A parameterized updraft method for calculating cloud densities in one-dimensional models. *Icarus* **245**, 273–281 (2015). doi:10.1016/j.icarus.2014.09.042

8. Marco Vedovato constructed groundbased optical Jupiter maps (from images taken by Christopher Go, Tadashi Horiuchi, Michel Jacquesson, Manos Kardasis, John Rozakis, Ian Sharp, Joost Verheyden, and Sean Walker) using Grischa Hahn's WinJupos software, available from http://jupos.org.

9. J. J. Lissauer, I. de Pater, *Fundamental Planetary Science* (Cambridge Univ. Press) (2013).

10. A. J. Friedson, Water, ammonia, and H_2S mixing ratios in Jupiter's five-micron hot spots. A dynamical model. *Icarus* **177**, 1–17 (2005). doi:10.1016/j.icarus.2005.03.004

11. A. P. Showman, T. E. Dowling, Nonlinear simulations of Jupiter's 5-micron hot spots. *Science* **289**, 1737–1740 (2000). Medline

12. I. de Pater, L. N. Fletcher, S. H. Luszcz-Cook, D. DeBoer, B. Butler, H. B. Hammel, M. L. Sitko, G. Orton, P. S. Marcus, Neptune's global circulation deduced from multi-wavelength observations. *Icarus* **237**, 211–238 (2014).

13. M. Asplund, N. Grevesse, A. J. Sauval, P. Scott, The chemical composition of the Sun. *Annu. Rev. Astron. Astrophys.* **47**, 481–522 (2009). doi:10.1146/annurev.astro.46.060407.145222

14. G. F. Lindal, The atmosphere of Neptune: An analysis of radio occultation data acquired with Voyager 2. *Astron. J.* **103**, 967–982 (1992). doi:10.1086/116119

15. R. A. Perley, C. J. Chandler, B. J. Butler, J. M. Wrobel, The Expanded Very Large Array: A new telescope for new science. *Astrophys. J.* **739**, L1 (2011). doi:10.1088/2041-8205/739/1/L1

16. X. S. Asay-Davis, P. S. Marcus, M. H. Wong, I. de Pater, Changes in Jupiter's zonal velocity between 1979 and 2008. *Icarus* **211**, 1215–1232 (2011). doi:10.1016/j.icarus.2010.11.018

17. J. L. Ortiz, G. S. Orton, A. J. Friedson, S. T. Stewart, B. M. Fisher, J. R. Spencer, Evolution and persistence of 5-μm hot spots at the Galileo probe entry latitude. *J. Geophys. Res.* **103**, 23051–23069 (1998). doi:10.1029/98JE00696

18. K. H. Baines, R. W. Carlson, L. W. Kamp, Fresh ammonia ice clouds in Jupiter. I. Spectroscopic identification, spatial distribution, and dynamical implications. *Icarus* **159**, 74–94 (2002). doi:10.1006/icar.2002.6901

19. M. H. Wong, I. de Pater, X. Asay-Davis, P. S. Marcus, C. Y. Go, Vertical structure of Jupiter's Oval BA before and after it reddened: What changed? *Icarus* **215**, 211–225 (2011). doi:10.1016/j.icarus.2011.06.032

20. R. A. Perley, B. J. Butler, An accurate flux density scale from 1 to 50 GHz. *Astrophys. J.* **204** (suppl.), 19 (2013). doi:10.1088/0067-0049/204/2/19

21. M. C. H. Wright, R. J. Sault, Mapping Cygnus A at 3 millimeter wavelength with the MIRIAD system. *Astrophys. J.* **402**, 546–549 (1993). doi:10.1086/172156

22. J. Gibson, Wm. J. Welch, I. de Pater, Accurate Jovian flux measurements at λ1cm show ammonia to be sub-saturated in the upper atmosphere. *Icarus* **173**, 439–446 (2005). doi:10.1016/j.icarus.2004.06.020

23. M. J. Klein, S. Gulkis, Jupiter's atmosphere—observations and interpretation of the microwave spectrum near 1.25-cm wavelength. *Icarus* **35**, 44–60 (1978). doi:10.1016/0019-1035(78)90059-3

24. J. L. Weiland, N. Odegard, R. S. Hill, E. Wollack, G. Hinshaw, M. R. Greason, N. Jarosik, L. Page, C. L. Bennett, J. Dunkley, B. Gold, M. Halpern, A. Kogut, E. Komatsu, D. Larson, M. Limon, S. S. Meyer, M. R. Nolta, K. M. Smith, D. N. Spergel, G. S. Tucker, E. L. Wright, Seven-year Wilkinson microwave anisotropy probe (WMAP) observations: Planets and celestial calibration sources. *Astrophys. J.* **192** (suppl.), 19 (2011). doi:10.1088/0067-0049/192/2/19

25. I. de Pater, M. Schulz, S. H. Brecht, Synchrotron evidence for Amalthea's influence on Jupiter's electron radiation belt. *J. Geophys. Res.* **102**, 22,043–22,064 (1997). doi:10.1029/97JA00311

26. I. de Pater, B. J. Butler, D. A. Green, R. Strom, R. Millan, M. J. Klein, M. K. Bird, O. Funke, J. Neidhöfer, R. Maddalena, R. J. Sault, M. Kesteven, D. P. Smits, R. Hunstead, Jupiter's radio spectrum from 74 MHz up to 8 GHz. *Icarus* **163**, 434–448 (2003). doi:10.1016/S0019-1035(03)00067-8